

Oriented Speckle Reducing Anisotropic Diffusion

Karl Krissian, *Member, IEEE*, Carl-Fredrik Westin, *Member, IEEE*, Ron Kikinis,
and Kirby Vosburgh, *Member, IEEE*.

Abstract—Ultrasound imaging systems provide the clinician with non-invasive, low cost, and real-time images that can help them in diagnosis, planning and therapy. However, although the human eye is able to derive the meaningful information from these images, automatic processing is very difficult due to noise and artifacts present in the image. The Speckle Reducing Anisotropic Diffusion filter was recently proposed to adapt the anisotropic diffusion filter to the characteristics of the speckle noise present in the ultrasound images and to facilitate automatic processing of images. We analyze the properties of the numerical scheme associated with this filter, using a semi-explicit scheme. We then extend the filter to a matrix anisotropic diffusion, allowing different levels of filtering across the image contours and in the principal curvature directions. We also show a relation between the local directional variance of the image intensity and the local geometry of the image, which can justify the choice of the gradient and the principal curvature directions as a basis for the diffusion matrix. Finally, different filtering techniques are compared on a 2D synthetic image with two different levels of multiplicative noise and on a 3D synthetic image of a Y-junction, and the new filter is applied on a 3D real ultrasound image of the liver.¹

Index Terms—Filtering, Anisotropic Diffusion, Ultrasound, Local Statistics, Speckle.

Ultrasound is a low cost, non-invasive imaging modality that has proved effective for many medical applications. However, the coherent nature of ultrasound results in images with speckle noise that reduces its utility for less than highly trained users and also complicates image processing tasks such as feature segmentation.

We first give a background on the noise properties in ultrasound images and on the restoration techniques that we use for noise reduction. In section 2, we discuss the properties of the numerical scheme proposed initially by Yu and Acton, and propose a semi-explicit version, using the Jacobi scheme. In section 3, we investigate how to extend the SRAD filter to a matrix diffusion equation, allowing a directional filtering in the gradient and the principal curvature directions. We also find a theoretical link between the local directional variance of the image intensity in the principal curvature directions and their associated curvatures. In Section 4, we compare quantitatively different filters on synthetic two and three-dimensional images. Finally, we show examples of running our filter on real datasets and conclude.

Harvard Medical School Brigham and Women's Hospital Dep of Radiology Thorn 323 Boston, MA 02115 USA fax : (+1) 617-264-6887 emails: {karl,westin,kikinis}@bwh.harvard.edu; and CIMIT, Cambridge, MA, USA, email: kirby@bwh.harvard.edu

¹Portions of this work are sponsored by the US Department of the Army under DAMD 17-02-2-0006 and CIMIT. The information does not necessarily reflect the position of the government and no official endorsement should be inferred.

I. BACKGROUND

A. Model of the speckle noise for ultrasound images

We denote g the observed signal, n the noise introduced by the acquisition process and f the original signal without noise that we would like to restore. Many image acquisition protocols, such as magnetic resonance imaging, introduce additive noise, which is usually modeled by a Gaussian variable of zero mean and a given standard deviation.

$$g = f + n. \quad (1)$$

The acquisition of ultrasound images introduces a specific noise known as speckle. A generalized model of the speckle imaging, as proposed in [1], can be written as:

$$g = fn + m, \quad (2)$$

where n and m are respectively the multiplicative and additive components of the noise. It is generally accepted that the effect of additive noise (such as sensor noise) is very small compared with that of multiplicative noise, which leads to a simplified model:

$$g = fn. \quad (3)$$

The statistics of the speckle noise, modeled by n , can be categorized into different classes according to the number of scatterers per resolution cell also called the scatterer number density (SND), to their spatial distribution and to the characteristics of the imaging system.

In the case of many fine randomly distributed scatterers per resolution cell (> 10) the speckle can be modeled by a Rayleigh distribution [2], [3] with a constant Signal to Noise Ratio (SNR) of 1.92. A generalized version of the Rayleigh distribution, the K distribution, must be used when the scatterer densities are smaller [4], [5], [6]. When the signal is corrupted with noise, the Rician model [7] can be used for high SNR and the Homodyne (or generalized) K-distribution [8] for lower SNR. The last generalizes the previous models. More analytic models have been proposed recently, including the Rician inverse Gaussian [9], Nakagami inverse Gaussian [10], the generalized Nakagami distribution [11] and correlated speckle patterns. Hence, an accurate description of the speckle statistics is still an area of active investigation and it involves complex analytical models.

Another characteristic of displayed ultrasound images is logarithmic compression, used to reduce the dynamic range of the input echo signal to match the smaller dynamic range of the display device and to emphasize objects with weak backscatter. Several investigators [12], [13], [14] have addressed the analytic study of log compressed Rayleigh signals in medical ultrasound images.

In the scope of this paper, we focus in reducing the noise of regions of fully formed speckle before logarithmic compression, where the speckle statistics can be modeled by a Rician distribution. In case of high SNR, the Rician distribution can be approximated by a Gaussian distribution, and we will follow this hypothesis.

Another property of the speckle is its spatial correlation as described in [2]. However, we will assume it is uncorrelated as in several previous works [15], [16], [17], [18]. In practice, this limitation may be addressed by applying specific pre-processing, as described in [19] or [20], and should result in an improvement of the proposed technique.

B. Previous works on Speckle reduction

Several approaches have been proposed to reduce the speckle effect in Synthetic Aperture Radar (SAR) images and Ultrasound images. Early works include the use of Linear Minimum Mean Square Error (LMMSE) [21], [22], [23]. More recent work proposes the use of wavelets [24] and of anisotropic diffusion [18], [15], [17], [25]. In most cases, the corrected image \hat{f} is calculated through a series of iterations. From a practical perspective, the most useful filtering approach combines an accurate estimator for \hat{f} with a stable iterative behavior.

1) *Local Linear Minimum Mean Square Error (LLMMSE) approaches:* The filter proposed by Lee [21] was derived from the simple filter proposed by Wallis [26], where each pixel is required to have a “desirable” local mean m_d and a “desirable local variance” v_d , leading to the following procedure:

$$\hat{f} = m_d + \sqrt{\frac{v_d}{v_g}}(g - \bar{g}), \quad (4)$$

where \bar{g} denotes the local mean of the observed signal. Lee proposes to use similar algorithms based on mean-square error minimization under the assumptions of additive noise, multiplicative noise or combination of additive and multiplicative noise.

Kuan *et al.* [23] propose a more general approach, where the observation equation is written as:

$$g = Bf + n, \quad (5)$$

where g is the degraded observed image, f is the original signal, n is a zero mean noise that can be signal-dependent or signal-independent, and B is a blurring matrix.

We observe that in both cases (additive and multiplicative), the optimal filter is simply written as:

$$\hat{f} = \bar{g} + \frac{v_f}{v_g} \cdot (g - \bar{g}) = \bar{g} + k \cdot (g - \bar{g}), \quad (6)$$

with $k = \frac{v_f}{v_g}$, and where v_f is the local spatial variance of f and v_g the local variance of g , at the current pixel/(voxel) location.

In the case of a scalar (point) processor, without any blurring ($B = I$), and uncorrelated additive noise, the LLMMSE filter gives (6) with (for any pixel (i, j)):

$$v_g = v_f + \sigma_n^2, \quad (7)$$

where σ_n^2 is the non-stationary noise variance and v_f is estimated from the relation $v_f = v_g - \sigma_n^2$. This filter is the same as the one derived by Lee for the additive case. However, in the multiplicative case, Kuan *et al.* derive the exact LLMMSE filter without the linear assumption made by Lee. In the case of multiplicative noise $g = nf$, where the noise n is independent of f , with stationary mean 1 and stationary standard deviation σ_n , the filter is (6), with (for any pixel (i, j)):

$$v_g = v_f + \sigma_n^2 (\bar{f}^2 + v_f) \quad (8)$$

or ($\bar{f} = \bar{g}$):

$$v_f = \frac{v_g - \sigma_n^2 \bar{g}^2}{1 + \sigma_n^2}. \quad (9)$$

The difference between the Kuan and the Lee filter for multiplicative noise is that the Lee filter would use the value $k_L = \frac{v_f}{v_f + \sigma_n^2 \bar{g}^2} = \frac{v_f}{v_g - \sigma_n^2 v_f}$ while the Kuan filter would use $k_K = \frac{v_f}{v_g}$.

2) *Speckle Reducing Anisotropic Diffusion:* Yu and Acton [16] compared the Lee filter with the anisotropic diffusion filter proposed by Perona and Malik, leading to a modified anisotropic diffusion that they call Speckle Reducing Anisotropic Diffusion (SRAD). They notice that (6) can be written as:

$$\hat{f} = g + (1 - k) \cdot (\bar{g} - g), \quad (10)$$

and, if we compute the mean from the 4 direct neighbors in 2D images, we can consider that $\bar{g} - g$ is an approximation of the Laplacian operator $\frac{1}{4} \text{div}(\nabla g)$, which allows considering the similarity between Lee or Kuan’s filter with the Partial Derivative Equation (PDE):

$$\begin{cases} u(0) = g \\ \frac{\partial u}{\partial t} = (1 - k) \text{div}(\nabla u), \end{cases} \quad (11)$$

where k is also a function of the diffusion time t . The anisotropic diffusion equivalent, where the diffusion coefficient is inside the divergence operator, can be written as:

$$\begin{cases} u(0) = g \\ \frac{\partial u}{\partial t} = \text{div}((1 - k) \nabla u) \\ = (1 - k) \text{div}(\nabla u) + \nabla(1 - k) \cdot \nabla u. \end{cases} \quad (12)$$

This last equation can be considered as a version of Perona and Malik filter, where the diffusion is controlled by the local statistics in the image, rather than by an additional chosen parameter. In this case, if the observed local standard deviation is characteristic of the noise ($v_f \rightarrow 0$ and $k \rightarrow 0$), we are in an homogeneous region and apply the heat equation. If not, k is closer to 1, we reduce the filtering and the filter can also have enhancing effect close to the contours, where $(1 - k)$ reaches a local minimum.

Compared to Perona and Malik’s anisotropic diffusion, the SRAD has the advantage of avoiding the threshold on the norm of the gradient needed for the diffusion function. This threshold is replaced by an estimation of the standard deviation of the noise at each iteration which gives to SRAD the following advantages:

- One less independent parameter,

- Less dependence on the norm of the gradient which can vary in the image,
- A natural decrease of the diffusion as the estimated standard deviation of the noise decreases: as $\sigma_n \rightarrow 0$, $v_f \rightarrow v_g$ and $(1 - k) \rightarrow 0$; so computations converge without smoothing out interesting features of the image.

3) *SRAD diffusion term*: Yu and Acton denote $C_u^2 = C_n^2 = \frac{\sigma_n^2}{\bar{n}^2} = \sigma_n^2$, where \bar{n} is the mean value of the noise and σ_n its standard deviation (we will use C_n instead of C_u because we denote the noise by n and u will be used to describe the image evolving under a Partial Differential Equation) and $C_{i,j}^2 = C^2 = \frac{v_g}{\bar{g}^2}$. (9) can then be written as:

$$\frac{v_f}{f^2} = \frac{C^2 - C_n^2}{1 + C_n^2} = \frac{1 + C^2}{1 + C_n^2} - 1. \quad (13)$$

Here, $q(t)$ is the discrete version of C and $q_0(t)$ the discrete version of C_n , which needs to be estimated at each iteration. They choose to apply the diffusion equation $\frac{\partial u}{\partial t} = \text{div}(c(q)\nabla u)$, where:

$$c(q) = \frac{1}{1 + \frac{q^2 - q_0^2}{q_0^2(1 + q_0^2)}}, \quad (14)$$

or

$$c(q) = e^{-\frac{q^2 - q_0^2}{q_0^2(1 + q_0^2)}}. \quad (15)$$

As noted by [17], using (14) is equivalent to using a discrete version of the equation $\text{div}((1 - k_L)\nabla u)$.

$$1 - k_L = 1 - \frac{v_f}{v_f + \sigma_n^2 \bar{g}^2} = \frac{\sigma_n^2 \bar{g}^2}{v_f + \sigma_n^2 \bar{g}^2} \quad (16)$$

$$= \frac{C_n^2}{(C^2 - C_n^2)/(1 + C_n^2) + C_n^2} = \frac{1}{1 + (C^2 - C_n^2)/[C_n^2(1 + C_n^2)]}. \quad (17)$$

The equivalent using Kuan's filter is (as mention in [17]):

$$1 - k_K = 1 - \frac{v_f}{v_g} = \frac{1 + 1/C^2}{1 + 1/C_n^2}. \quad (18)$$

4) *Detail Preserving Anisotropic Diffusion*: In a recent study, Aja-Fernández and Alberola-López [17] modify the SRAD filter to rely on the Kuan filter rather than the Lee filter, i.e to change k_L to k_K in the diffusion equation. They call this modified approach the Detail Preserving Anisotropic Diffusion (DPAD). They further estimate the local statistics using a larger neighborhood than the 4 direct neighbors used by Yu and Acton, showing that better results and better stability can be obtained using a 5×5 neighborhood. For the estimation of C_n , they use a median based estimator C_{med}^2 or C_{MAD}^2 , which was proposed in [15].

C. Flux Anisotropic Diffusion

The anisotropic diffusion equation can be written as:

$$\begin{cases} u(x, 0) &= u_0 \\ \frac{\partial u}{\partial t} &= \text{div}(\mathbf{F}) + \beta(u_0 - u), \end{cases} \quad (19)$$

where \mathbf{F} is the diffusion flux and β is a data attachment coefficient.

If $\beta = 0$, particular cases of this equation are:

- the heat diffusion equation $\mathbf{F} = \nabla u$ which is equivalent to a Gaussian convolution;
- the Perona and Malik equation [27] with $\mathbf{F} = \varphi(|\nabla u|)\nabla u$ where φ is a diffusion function. This function has the effect of reducing the diffusion for 'high' gradients, based on a *threshold* δ on the norm of the gradient.
- the matrix diffusion proposed in [28], which uses a diffusion matrix noted D with a flux $\mathbf{F} = D\nabla u$.

The matrix D can be expressed in a diagonal form, with eigenvectors ($\mathbf{v}_0, \mathbf{v}_1, \mathbf{v}_2$) and eigenvalues $\lambda_0, \lambda_1, \lambda_2$. Then the flux can be expressed as

$$\mathbf{F} = D\nabla u = \sum_{i=0}^2 \lambda_i u_{\mathbf{v}_i} \mathbf{v}_i, \quad (20)$$

where $u_{\mathbf{v}_i} = \nabla u \cdot \mathbf{v}_i$ is the first order derivative of the intensity in the direction of \mathbf{v}_i . In [29], we use a particular flux that is decomposed in the basis of the gradient (\mathbf{v}_0) and the maximal (\mathbf{v}_1) and minimal (\mathbf{v}_2) curvature directions computed on the smoothed image u^* , where the smoothing is obtained by convolution with a Gaussian of standard deviation σ . The principal curvature directions are computed as two eigenvectors of the matrix $PH_\sigma P$ where H_σ is the Hessian matrix of the image u^* and P is the projection matrix orthogonal to the gradient direction, that is $H' = PH_\sigma P$ with $P = I - \left(\frac{\nabla u^*}{|\nabla u^*|}\right) \cdot \left(\frac{\nabla u^*}{|\nabla u^*|}\right)^t$, where I is the identity matrix in 3D. The eigenvalues of the diffusion matrix are chosen as functions of the first order derivative of the intensity in the corresponding eigenvector direction, and can be written in the form $\lambda_i(u_{\mathbf{v}_i}) = u_{\mathbf{v}_i} \cdot \varphi_i(u_{\mathbf{v}_i})$. The diffusion in the gradient direction, $\varphi_0(x)$, is chosen as Perona and Malik's diffusion function, i.e $\varphi_0(x) = e^{-\frac{x^2}{\delta^2}}$ where δ is a threshold on the intensity derivative in the smoothed gradient direction, and $0 < \varphi_1 \leq \varphi_2 \leq 1$ weight the diffusion in the principal curvature directions.

The data attachment term was first introduced by Nordström [30], who proposed to unify the variational methods of energy minimization [31], [32] with the anisotropic diffusion equation introduced by Perona and Malik. This term allows a convergence of the diffusion scheme to an image that remains close to the initial data. It regularizes the equation, permitting its expression as an optimal solution and obviates the need to choose a diffusion time for stopping iterations.

1) Constraining the noise properties during the diffusion:

The properties of the noise (mean and standard deviation), can be used to constrain the diffusion process. This approach was proposed in [33] for additive noise. In [34], we propose to adapt this approach for ultrasound images using the Loupas model for the speckle statistics. In [25], Rudin *et al.* extend their initial technique to deal with multiplicative noise and blur in the image. However, in our experiments, no clear improvement was obtained by adding the constraints to the Partial Differential Equation proposed in [25] in the case of multiplicative noise. Results are depicted in Tables V, VI and VIII, for the Rudin *et al.* and Rudin *et al. attach.* methods, where the constraints lead similar or worse results. For this

reason, we don't extend our current approach by adding these constraints.

II. NUMERICAL SCHEMES

We denote $c(\mathbf{x}, t) = c(q(\mathbf{x}, t), q_0(t)) = 1 - k(q(\mathbf{x}, t), q_0(t))$ the diffusion coefficient, where q is a discrete approximation of C and $q_0(t)$ is an estimate of C_n at time t . The Partial Differential Equation can be discretized using an explicit scheme:

$$u^{k+1}(\mathbf{x}) = u^k(\mathbf{x}) + dt \operatorname{div}(c \nabla u) \quad (21)$$

$$u^{k+1}(\mathbf{x}) = u^k(\mathbf{x}) + dt \sum_{\mathbf{n} \in \eta} c_{\mathbf{n}}^k (u^k(\mathbf{n}) - u^k(\mathbf{x})) \quad (22)$$

$$= \left(1 - dt \sum_{\mathbf{n} \in \eta} c_{\mathbf{n}}^k\right) u^k + dt \sum_{\mathbf{n} \in \eta} c_{\mathbf{n}}^k u^k(\mathbf{n}) \quad (23)$$

where η is the neighborhood of the point \mathbf{x} consisting in the direct neighbors in each direction (typically 4 neighbors in 2D and 6 in 3D, but diagonal neighbors could be added as proposed in [35]), $c_{\mathbf{n}}^k(\mathbf{x}) = \frac{c^k(\mathbf{n}) + c^k(\mathbf{x})}{2}$ is the mean value of the diffusion coefficient between the position \mathbf{x} and its neighbor pixel \mathbf{n} .

A. Stability

Following the approach of Weickert [28], [36], we can write the discrete scheme in the form:

$$\begin{cases} \forall k \in [0, +\infty[, & \mathbf{u}^0 = f \\ & \mathbf{u}^{k+1} = Q(\mathbf{u}^k) \mathbf{u}^k, \end{cases} \quad (24)$$

where \mathbf{u}^k is the image represented as a vector of size the total number of pixels (/voxels) of the image, denoted n , and $Q(\mathbf{u}^k)$ is a $n \times n$ matrix. The author derives 6 criteria for the matrix Q to ensure good properties like maximum-minimum principle and convergence to a constant steady state. These properties are:

- D1 Continuity in its arguments ($Q \in C(\mathbb{R}^n, \mathbb{R}^n \times \mathbb{R}^n)$);
- D2 Symmetry ($q_{ij} = q_{ji}$);
- D3 Unit Row Sum ($\sum_j q_{ij} = 1$);
- D4 Nonnegativity ($q_{ij} \geq 0$);
- D5 Positive Diagonal ($q_{ii} > 0$) and
- D6 Irreducibility (any 2 pixels can be connected by a path with nonvanishing diffusivities).

D1 is ensured because the coefficients $c = 1 - k$ are continuous functions of the image, **D2** is true because the non-diagonal coefficients $q_{ij} = q_{ji}$ are defined by $\frac{c_i + c_j}{2}$ (however, this property is not satisfied in the original numerical scheme proposed by Yu and Acton, where $c_{\mathbf{n}}(\mathbf{x}) = c(\mathbf{n})$), **D3** is satisfied, **D4** and **D5** are satisfied if and only if $1 - dt \sum_{\mathbf{n} \in \eta} c_{\mathbf{n}}^k(\mathbf{x}) > 0$ for any pixel position \mathbf{x} , and **D6** is satisfied because both diffusion function $1 - k_L$ and $1 - k_K$ are strictly positive, so $\forall i \neq j, q_{ij} > 0$ and we can always find a path through between 2 pixels using the 4 direct neighbors (the same reasoning is also valid in three or more dimensions).

To summarize, the good properties of the explicit scheme are satisfied if

$$dt^{k+1} < \frac{1}{|\eta| \max_{\mathbf{x}} c^k(\mathbf{x})}, \quad (25)$$

TABLE I
COMPARISON OF THE DIFFUSION FUNCTIONS BASED ON LEE AND KUAN'S FILTERS.

Function	Limit at 0^+	Value at C_n	Limit at $+\infty$
$1 - k_L$	$1 + \frac{1}{C_n^2}$	1	0
$1 - k_K$	$+\infty$	1	$\frac{C_n^2}{1 + C_n^2}$

where $|\eta|$ is the size of the neighborhood, typically 4 in 2D images and 6 in 3D images.

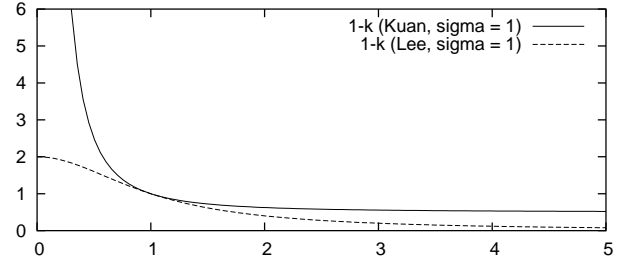


Fig. 1. Comparison of Lee's and Kuan's diffusion as functions of C , for $C_n = 1$.

In Fig. 1 and Table I, we show the behavior of the two functions $1 - k_L(C)$ and $1 - k_K(C)$. We see that $1 - k_L$ is bounded by $1 + 1/C_n^2$, which gives a limit condition for the choice of dt , but the function $1 - k_K$ is not bounded as it tends to $+\infty$ as C tends to 0. However, using a semi-explicit scheme can ensure stability for both functions.

B. Semi-explicit scheme for SRAD and DPAD

The diffusion equation is often discretized using the Jacobi or Gauss-Seidel schemes. Another possible scheme is Additive Operator Splitting (AOS) [37], [36], [28]. In [36], the performance of the explicit scheme, the Gauss-Seidel scheme, and AOS are compared in terms of processing time versus accuracy. The authors show that depending on the level of accuracy needed, the explicit scheme can be the best choice (less than 1% error), with the Gauss-Seidel between 1% and 1.7% and the AOS scheme for errors more than 1.7%. Because we desire a good trade-off among ease of implementation, speed and accuracy, we use the Jacobi scheme, which is slower than Gauss-Seidel but has the advantage of being symmetric (while the Gauss-Seidel scheme depends on the order that we traverse the image). The Jacobi approach has also the advantage of being straightforward to parallelize using a multi-threading approach while the Gauss-Seidel scheme, being recursive, does not allow straightforward parallelization. The Jacobi numerical scheme is written as:

$$u^{k+1}(\mathbf{x}) = u^k(\mathbf{x}) + dt \sum_{\mathbf{n} \in \eta} c_{\mathbf{n}}^k (u^k(\mathbf{n}) - u^{k+1}(\mathbf{x})) \quad (26)$$

or:

$$u^{k+1}(\mathbf{x}) = \frac{u^k(\mathbf{x}) + dt \sum_{\mathbf{n} \in \eta} c_{\mathbf{n}}^k u^k(\mathbf{n})}{1 + dt \sum_{\mathbf{n} \in \eta} c_{\mathbf{n}}^k}, \quad (27)$$

This new scheme follows all properties **D1-6** listed previously apart from the symmetry of the matrix Q (property **D2**). We

also notice that the positivity of the diagonal elements (**D5**) is unconditionally satisfied. In practice, this scheme possesses very good stability for any time step dt . Thus, it allows the use of Kuan's function, and the processing time of one iteration compared to the explicit scheme is comparable (one more division per pixel or voxel). The parallel between (10) and (11), based on $\bar{g} - g \approx \frac{1}{|\eta|} \text{div}(g)$ would suggest the use of the value $dt = 1/|\eta|$ as a constant time step.

III. DIRECTIONAL SRAD

A. Matrix extension based on the Flux Diffusion

By combining the approaches of Yu and Acton with a matrix anisotropic diffusion (we use the Flux Diffusion in this case), we add an additional feature to the SRAD filter, to better restore of the image. The concept is to add to the SRAD filter a non-scalar component which can perform directional filtering of the image along the structures. We seek the same kind of improvement that matrix anisotropic diffusion adds to standard scalar anisotropic diffusion. Formally, SRAD is written as:

$$\begin{aligned} \frac{\partial u}{\partial t} &= \text{div}((1-k)\nabla u) \\ &= \text{div} \left(\begin{bmatrix} 1-k & \cdot & \cdot \\ \cdot & 1-k & \cdot \\ \cdot & \cdot & 1-k \end{bmatrix} \nabla u \right), \end{aligned} \quad (28)$$

where ' \cdot ' denotes zero. The diffusion matrix is a scalar, so it can be written as $D = (1-k)I$, where I is the identity matrix. In the case of the flux diffusion, we use the directions of the gradient and principal curvature directions on a smoothed version of the image. Alternatively, one might use the eigenvectors of the structure tensor as proposed in [28], [38], or combine first and second order derivatives by combining the structure tensor and the Hessian matrix as proposed in [39], [40]. We can take advantage of the local orientation to enforce more coherence of the structures along directions of minimal intensity change. From our previous experience, the combination of enhancement in the gradient direction with smoothing in the minimal curvature direction can lead very good enhancement of tubular structures like blood-vessels in 3D images. The new diffusion matrix can be written, in the basis $(\mathbf{v}_0, \mathbf{v}_1, \mathbf{v}_2)$, as

$$D = \begin{bmatrix} 1-k & \cdot & \cdot \\ \cdot & c_{max} & \cdot \\ \cdot & \cdot & c_{min} \end{bmatrix}, \quad (29)$$

where c_{max} is the amount of smoothing along the direction of maximal curvature, and c_{min} is the amount of smoothing along the direction of minimal curvature. For 2D images, only one coefficient c_{tang} is used. In the case of the flux diffusion, we use $c_{min} \gg c_{max}$, and we can use for example $c_{max} = 0$ and $c_{min} = 1$. We call this new filter Oriented Speckle Reducing Anisotropic Diffusion, and we will denote it as OSRAD.

B. Relation between the local variance and the local geometry

Let us suppose that the image is locally smooth and has smooth 1st and 2nd order derivatives in all directions. We can

then write the second order Taylor expansion of the image as:

$$u(\mathbf{x} + h\mathbf{v}) = u(\mathbf{x}) + h\mathbf{v}^t \nabla u + \frac{1}{2} h^2 \mathbf{v}^t H \mathbf{v} + o(h^2), \quad (30)$$

where \mathbf{v} is a unit vector, $h \ll 1$ is a small real number, ∇u is the gradient vector of the image at \mathbf{x} , and H is the Hessian matrix of the image at \mathbf{x} .

Now, the local mean and local variance of the image in the direction \mathbf{v} may be written as:

$$m_{\mathbf{v}}(u, \mathbf{x}) = \frac{1}{2A} \int_{-A}^A u(\mathbf{x} + h\mathbf{v}) dh, \quad \text{and} \quad (31)$$

$$V_{\mathbf{v}}(u, \mathbf{x}) = \frac{1}{2A} \int_{-A}^A (u(\mathbf{x} + h\mathbf{v}) - m_{\mathbf{v}}(u, \mathbf{x}))^2 dh \quad (32)$$

If we take instead a Gaussian weighted mean and variance, with a Gaussian of standard deviation σ , we can define:

$$m_{\mathbf{v},\sigma}(u, \mathbf{x}) = \frac{1}{\sqrt{2\pi}\sigma} \int_{-\infty}^{+\infty} G_{\sigma}(h) u(\mathbf{x} + h\mathbf{v}) dh \quad \text{and} \quad (33)$$

$$V_{\mathbf{v},\sigma}(u, \mathbf{x}) = \frac{1}{\sqrt{2\pi}\sigma} \int_{-\infty}^{+\infty} G_{\sigma}(h) (u(\mathbf{x} + h\mathbf{v}) - m_{\mathbf{v},\sigma})^2 dh, \quad (34)$$

where $m_{\mathbf{v},\sigma} = m_{\mathbf{v},\sigma}(u, \mathbf{x})$. We call the first expressions $V_{\mathbf{v}}$ and $m_{\mathbf{v}}$ the uniform case and the second ones $V_{\mathbf{v},\sigma}$ and $m_{\mathbf{v},\sigma}$ the Gaussian case. Using the second order Taylor expansion (see Appendix):

$$m_{\mathbf{v}} \approx u(\mathbf{x}) + \frac{A^2}{6} \mathbf{v}^t H \mathbf{v} \quad (35)$$

$$V_{\mathbf{v}} \approx \frac{A^2}{3} \mathbf{v}^t \nabla u \cdot \nabla u^t \mathbf{v} + \frac{A^4}{45} \mathbf{v}^t H \mathbf{v} \mathbf{v}^t H \mathbf{v} \quad (36)$$

$$m_{\mathbf{v},\sigma} \approx u(\mathbf{x}) + \frac{\sigma^2}{2} \mathbf{v}^t H \mathbf{v} \quad (37)$$

$$V_{\mathbf{v},\sigma} \approx \sigma^2 \mathbf{v}^t \nabla u \cdot \nabla u^t \mathbf{v} + \frac{\sigma^4}{2} \mathbf{v}^t H \mathbf{v} \mathbf{v}^t H \mathbf{v} \quad (38)$$

Remark: At first order, the local directional variance in the direction \mathbf{v} is directly proportional to the square of the scalar product of \mathbf{v} and ∇u , so in the gradient direction, it is proportional to the square of the norm of the gradient $|\nabla u|^2$.

If we now consider the plane orthogonal to the gradient, any vector in this plane will have the first term null: $\forall \mathbf{v} \perp \nabla u, \mathbf{v}^t \nabla u \nabla u^t \mathbf{v} = 0$, so the directional local variance will only depend on the Hessian matrix for a 2nd order approximation of the image:

$$\forall \mathbf{v} \perp \nabla u, V_{\mathbf{v}} = \beta' (\mathbf{v}^t H \mathbf{v})^2, \quad (39)$$

where β' is either $\frac{A^4}{45}$ or $\frac{\sigma^4}{2}$.

$\mathbf{v}^t H \mathbf{v}$ expressed at \mathbf{x} is equivalent to the second order derivative of the image u in the direction \mathbf{v} at \mathbf{x} , that we can also write $u_{\mathbf{v}\mathbf{v}}(\mathbf{x})$. The principal directions of curvature are the eigenvectors of the projection of the matrix H in the plane orthogonal to the gradient, denoted H' :

$$H' = \left(I - \frac{\nabla u \cdot \nabla u^t}{|\nabla u|^2} \right)^t H \left(I - \frac{\nabla u \cdot \nabla u^t}{|\nabla u|^2} \right). \quad (40)$$

If we consider, in a N -dimensional image, the principal directions of curvature $\mathbf{v}_1, \dots, \mathbf{v}_{N-1}$ and the associated curvatures of the isosurface of the image passing through the point \mathbf{x} , $\kappa_1, \dots, \kappa_{N-1}$, where we define the normalized gradient as the normal of the isosurface, the following relation holds:

$$\forall j \in [1, N-1], u_{\mathbf{v}_j \mathbf{v}_j} = \mathbf{v}_j^t H' \mathbf{v}_j = \mathbf{v}_j^t H \mathbf{v}_j = -|\nabla u| \kappa_j. \quad (41)$$

Thus, we obtain a relation between the local variance in the direction of a principal curvature and the associated curvature as:

$$\forall j \in [1, N-1], V_{\mathbf{v}_j} = \beta' |\nabla u|^2 \kappa_j^2. \quad (42)$$

In summary, we presented in this section a directional speckle reducing anisotropic diffusion and an interpretation of the oriented local statistics at the contours of the structures in a non-noisy image. We will use the matrix extension based on the flux diffusion proposed in section III-A for our experiments. The relations that we have derived between the local directional variance in a principal curvature direction and the associated curvature helps understanding the contribution of the local geometry to the local intensity variance.

IV. EXPERIMENTS AND RESULTS

We first list the parameters of the filter and discuss the different choices available for each parameter and their sensitivity. We then present results on one two-dimensional synthetic image with two levels of multiplicative noise, one three-dimensional synthetic image with two levels of multiplicative noise and one real three-dimensional dataset of a human liver, reconstructed from 2D sections. To quantify the results on synthetic images, we use the same approach as [16], which consists in measuring the mean and standard deviation on different homogeneous regions of the image, and measuring the quality of the contours using Pratt's figure of merit.

A. Parameters and choices of the filter

The filter has the following parameters or choices: 1) the coefficient of variation of the noise q_0 , 2) the numerical scheme, 3) the time step dt , 4) the number of iteration, or a convergence criterion, 5) the diffusion function: Lee or Kuan, 6) the size of the neighborhood used to compute the coefficients of variation.

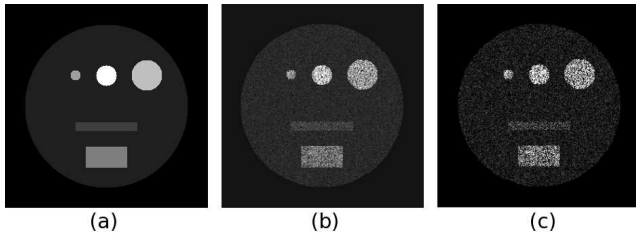


Fig. 2. Synthetic 2D image. (a) the original image, (b) the original image with multiplicative noise of mean 1 and standard deviation 0.5 (c) the original image with multiplicative noise of mean 1 and standard deviation 1.

1) *Computation of the noise statistics q_0* : At each iteration, $q_0(t)$ is an important parameter to estimate, since it drives the quantity of diffusion that is locally applied. It can be

computed from the mean and the standard deviation of a region specified by the user, from the median of the local coefficients of variation with a given neighborhood as proposed in [17], or it could also be estimated using the local directional covariance matrix. Because we want to reduce the manual interaction as much as possible, we will use the median of the local coefficients of variation. The option of using the local directional covariance matrix should be studied in future work, where the local variance of the noise in the direction of minimal noise variance can be used to improve the robustness of $q_0(t)$ with respect to contours.

We will use the 2D synthetic image of Fig. 2, where the initial image contains different circular or rectangular regions of different intensities. This image is corrupted with multiplicative Gaussian noise of mean 1 and standard deviation 0.5 and 1.

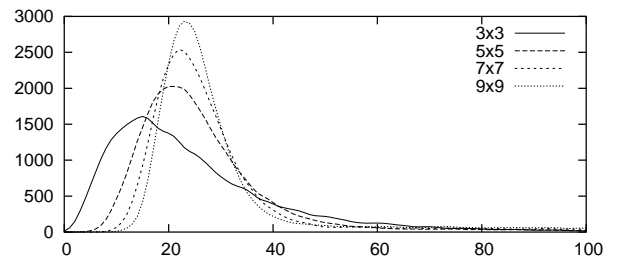


Fig. 3. Histograms, for different sizes of neighborhoods, of the coefficient of variation q_0^2 estimated on the synthetic image with multiplicative noise of $\sigma_n = 0.5$. The values in abscissa are magnified by 100.

Fig. 3 shows, on the synthetic image of Fig. 2 with multiplicative noise of standard deviation 0.5, the histograms of q_0^2 estimated using different sizes of neighborhood. Table II and III show the median values of q_0 for the synthetic 2D images with multiplicative noise of $\sigma_n = 0.5$ and $\sigma_n = 1$ and different sizes of neighborhood, using either discrete neighborhood or Gaussian weighting. Some high values of q_0^2 induced by the contours of the objects are not displayed in the histogram of Fig. 3 because they are higher than the maximal displayed value in X coordinates. However, those values contribute in increasing the standard deviation of q_0 and can interfere in the neighborhood of contours. Increasing the scale of the estimation of the local coefficient of variation q_0 both improves the estimation of q_0 in homogeneous regions and leads to an over-estimation in the vicinity of the contours.

TABLE II
MEDIAN VALUE OF q_0 ON THE SYNTHETIC NOISY IMAGE, NOTED med_1 ($/med_2$) FOR $\sigma_n = 0.5$ ($/1$). SD_1 ($/SD_2$) IS THE STANDARD DEVIATION OF q_0 CENTERED ON THE MEDIAN.

Neighborhood	2x2	3x3	5x5	7x7	9x9
med_1	0.396	0.457	0.493	0.503	0.509
SD_1	0.168	0.144	0.112	0.110	0.117
med_2	0.798	0.876	0.972	1.003	1.018
SD_2	0.356	0.318	0.261	0.221	0.204

The first effect will tend to lower the standard deviation of q_0 while the second effect will tend to increase it, sometimes leading to a minimum value of the standard deviation of q_0 .

TABLE III

MEDIAN VALUE OF q_0 ON THE SYNTHETIC NOISY IMAGE, NOTED med_1 ($/med_2$) FOR $\sigma_n = 0.5$ ($/1$). SD_1 ($/SD_2$) IS THE STANDARD DEVIATION OF q_0 CENTERED ON THE MEDIAN. THE LOCAL STATISTICS ARE COMPUTED USING GAUSSIAN WEIGHTS OF STANDARD DEVIATION σ .

σ	0.5	1	1.5	2	2.5	3	3.5
med_1	0.324	0.469	0.495	0.506	0.513	0.517	0.523
SD_1	0.122	0.126	0.110	0.110	0.118	0.127	0.136
med_2	0.580	0.888	0.964	0.997	1.017	1.028	1.039
SD_2	0.220	0.276	0.243	0.216	0.204	0.202	0.207

In Table II, the smallest standard deviations are reached for a 7×7 neighborhood when $\sigma_n = 0.5$ and for at least 9×9 neighborhood when $\sigma_n = 1$. In Table III, the smallest standard deviations are reached for standard deviations 1.5 and 2 when $\sigma_n = 0.5$, and for standard deviation 3 for $\sigma_n = 1$. The minimal standard deviation of q_0 does not always correspond to the best estimation of the local coefficient of variation and is not necessarily present in real ultrasound images, thus we cannot use it as a criterion to automatically select the best neighborhood. However, the neighborhood should increase with the variance of the noise. In their experiments, Aja-Ferández et al. [17] use a 5×5 neighborhood.

2) *Other parameters*: For the numerical scheme, we propose to use the semi-explicit scheme described in II-B, but we will also quantify results using an explicit scheme. For the time step and the number of iterations, we will use $dt = 0.05$ with 300 iterations in our experiments, for both the explicit and the semi-explicit schemes. It could also be interesting to use a convergence criterion based on the difference between two successive iterations. For the diffusion functions, we will use both the Lee and the Kuan functions in order to compare them. Since the diffusion is defined as $1 - k = 1 - \frac{v_f}{v_g}$, it can be argued that the estimated local variance of the image without noise v_f should always be positive and thus that the diffusion function should be limited to the interval $[0, 1]$. In practice, the standard deviation of the noise estimate is not perfect and limiting $1 - k$ can prevent taking into account local variations of intensity smaller than the estimated noise level. Thus, we allow any value of the diffusion function and in the case of the explicit scheme, we limit the time step to satisfy the stability criterion given by (25). The local coefficients of variation are computed using the 4 direct neighbors denoted N_4 , like the original SRAD, and using a 3×3 neighborhood denoted N_9 .

B. Synthetic 2D image

We ran different filters on the two noisy images of Fig. 2. The parameters of the filters are given in Table IV. The neighborhood column specifies the size of the neighborhood to compute local statistics and the standard deviation σ of a Gaussian smoothing (when needed). The threshold parameter is a threshold on the norm of the gradient used by anisotropic diffusion filters. The homotopic version of Perona and Malik filter consists in filtering the logarithm of the image and in applying the exponential function to the intensity of the filtered image. *Catté et al.* filter [41] is a version of anisotropic diffusion where the diffusion function is applied to a smoothed

version of the norm of the gradient of the image. For Lee filter and Kuan filter, the standard deviation of the noise σ_n is known. In the case of SRAD, PDAD and OSRAD filters, a region of interest of constant intensity was selected to compute an estimation of the coefficient $q_0(t)$. The neighborhoods N_4 and N_9 are respectively the four direct neighbors and the 3×3 neighborhood.

TABLE IV

PARAMETERS OF THE DIFFERENT FILTERS FOR THE SYNTHETIC 2D IMAGE.

Filter	Iter.	dt	Neighb.	Thres.	Scheme
Median	10	-	5×5	-	-
Lee and Kuan	1	-	7×7	-	-
P&M	300	0.1	-	4	expl.
Homotopic P&M	400	0.1	-	0.3	expl.
Catté et al.	300	0.1	$\sigma = 2$	1	expl.
Rudin et al.	3000	0.01	-	-	-
Rudin et al. attach	3000	0.01	-	-	expl.
Flux diffusion	200	0.05	$\sigma = 2$	1	expl.
SRAD and DPAD	200	0.05	N_4/N_9	-	expl. / impl.
OSRAD	200	0.05	$\sigma = 1$	2	impl.

The results for a noise of standard deviation 0.5 are shown in Fig. 4 and Table V, and the results for a noise of standard deviation 1 are shown in Table VI. We define 6 regions of constant intensity in the original image and compute the mean and the standard deviation of the intensity within each region on the filtered images. We denote f each filter to be tested, $f \in [1, N_f]$, where N_f is the total number of filters, in our case $N_f = 18$; r the index of a region, $r \in [1, 6]$; $m_{r,f}$ the mean intensity of the region r for the filter f , and $\sigma_{r,f}$ the associated standard deviation. We now define a distance $d_{r,f}$, which takes into account both the mean and the standard deviation for each region and each filter:

$$d_{r,f} = \max(|m_{r,f} + \sigma_{r,f} - m_r|, |m_{r,f} - \sigma_{r,f} - m_r|), \quad (43)$$

where m_r is the mean intensity of the region r computed on the noisy image. If the filter preserves the mean intensity of the object and creates constant regions, then the distances $d_{r,f}$ for this filter should be 0 for all regions. We then define a global measure M_f for each filter.

$$M_f = \prod_{r=1}^6 e^{-\frac{d_{r,f}^2}{2D_r^2}}, \quad (44)$$

where D_r is the average value of $d_{r,f}$ for a given region r and over all the filters f . The value M_f is comprised between 0 and 1, and measures the quality of the filter compared to the other filters used to restore our synthetic noisy images. The highest the value, the better the filter.

To estimate the quality of the contours, we use Pratt's figure of merit (FOM) [42] defined by (45).

$$FOM = \frac{1}{\max\{\hat{N}, N_{ideal}\}} \sum_{i=1}^{\hat{N}} \frac{1}{1 + d_i^2 \alpha}, \quad (45)$$

where \hat{N} and N_{ideal} are the number of detected and ideal edge pixels, and d_i is the Euclidean distance between the i^{th} edge pixel and the nearest ideal edge pixel, and α is a constant set to

0.9. The values range between 0 and 1, where 1 is equivalent to perfect edge detection. As proposed by [16], we use the Canny edge detector [43] with a standard deviation of 0.1 and a threshold of 0.5.

From Tables V and VI, we observe that our new technique, denoted “OSRAD”, have a better behavior for both measures in the case of a noise of standard deviation $\sigma_n = 1$. In the case of $\sigma_n = 0.5$, the last two lines of Table V are very similar with a measure of M_f almost equal, but a better measure of the Pratt’s Figure of Merit in the case of our technique (0.768 versus 0.731 for DPAD). A justification of this behavior is that the matrix formulation of the anisotropic diffusion allows a better preservation of the contours, and a significant difference between the filters can be noticed only in the case of a high noise level. While looking at both measures M_f and FOM , our new filter is more efficient than the other techniques on this synthetic image, especially in the case of a strong noise.

C. Synthetic 3D image

We created a synthetic 3D image representing a Y-junction of a vessel. The main vessel of radius 4 voxels splits into two branches forming an angle of 90 degrees and of radii 2 and 3 voxels. To simulate ultrasound acquisition, the intensity of the vessel is set to 25 and the intensity of the background is set to 50. The binary image is then convolved by a Gaussian kernel of standard deviation 0.7 to create a partial volume effect, and is multiplied by a Gaussian noise of mean 1 and of standard deviation 0.25. Quantitative results of the different filters are presented in Table VIII.

We used the parameters given in Table VII for each filter.

From both 2D and 3D experiments, summarized in Tables V, VI and VIII, we can deduce the following:

- the standard anisotropic diffusion introduced by Perona and Malik, as we expected, is not able to filter multiplicative noise, even when it is applied to the logarithm of the image (homotopic filter);
- we were not able to obtain better results using the multiplicative constraint proposed by Rudin et al. [25] as an extension to their previous filter [33].
- The implicit scheme for SRAD and DPAD lead to better results than the explicit numerical schemes, because they are able to create more homogeneous regions;
- DPAD gives slightly better results than SRAD.
- for both SRAD and DPAD, using 9 (or 27 in 3D) neighbors leads to better results than using 4 (or 6) neighbors;
- the flux diffusion, even if it is not adapted to multiplicative noise, leads to reasonable results;
- our new technique gives the best balance between the homogeneity of the region, the preservation of the original image intensity, and the quality of the contours.

Figure 5 presents the results of different filters, which give good values of M_f , FOM , or both. It shows the tendency of the flux diffusion to create elongated structures from noise of high standard deviation, the strong attenuation of the small vessel structure for Rudin et al.’s filter, the good restoration of DPAD

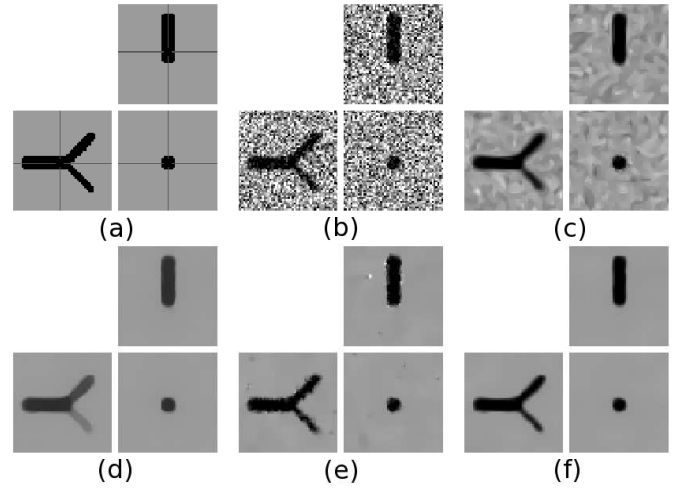


Fig. 5. Slice display from the 3D synthetic Y-junction image. From left to right and top to bottom: a) initial image, b) initial image with multiplicative noise of standard deviation 0.25, c) result of the flux diffusion, d) of Rudin et al.’s filter, e) of DPAD with implicit scheme and $3 \times 3 \times 3$ neighborhood and f) result of the new OSRAD filter.

filter but with remaining noise at the contours, and the good restoration of the proposed technique with smooth and sharp contours.

TABLE VIII
RESULTS ON NOISY SYNTHETIC 3D IMAGE WITH $\sigma = 0.25$.

	Vessels	Background	M1	FOM
Initial	25	50		1
Noisy image	24.94 ± 6.28	50.01 ± 12.49		0.072
Median	29.70 ± 3.43	49.96 ± 1.22	0.1	0.087
Lee	31.39 ± 3.80	49.92 ± 1.07	0.03	0.096
Kuan	31.50 ± 3.75	49.92 ± 1.06	0.03	0.096
P&M	26.22 ± 3.82	50.00 ± 12.20	0	0.097
homotopic P&M	26.18 ± 5.32	49.03 ± 7.55	0	0.109
Catté et al.	25.39 ± 5.84	49.99 ± 1.03	0.25	0.766
Flux	25.51 ± 2.36	50.00 ± 2.22	0.41	0.907
Rudin et al.	34.00 ± 2.68	49.91 ± 0.24	0.01	0.950
Rudin et al. att.	24.24 ± 4.77	48.47 ± 6.28	0	0.100
SRAD expl N_6	26.16 ± 2.67	49.99 ± 2.94	0.2	0.093
SRAD expl N_{27}	25.68 ± 3.16	49.99 ± 2.93	0.2	0.096
SRAD impl N_6	27.00 ± 2.05	49.98 ± 0.55	0.57	0.177
SRAD impl N_{27}	26.17 ± 2.45	49.99 ± 0.54	0.63	0.200
DPAD expl N_6	26.17 ± 2.66	49.99 ± 2.93	0.20	0.100
DPAD expl N_{27}	25.70 ± 3.13	49.99 ± 2.93	0.20	0.104
DPAD impl N_6	27.02 ± 2.05	49.98 ± 0.55	0.56	0.599
DPAD impl N_{27}	26.21 ± 2.42	49.99 ± 0.54	0.63	0.432
OSRAD	26.54 ± 2.04	50.00 ± 0.30	0.66	0.98

D. Real data set of the liver

A 3D ultrasound of a liver was acquired using a freehand system that consisted of a Lynx ultrasound unit (BK Medical Systems, Wilmington, MA) and a miniBIRD tracking device (Ascension Technology, Burlington, VT)². The 3D ultrasound was generated using the Stradx software (Cambridge University, Cambridge, UK) and the technique described in [44]. The image dimensions are $201 \times 193 \times 142$ with isotropic voxel resolution. We ran our filter with the following parameters: a time step $dt = 0.05$, 50 iterations, a Gaussian smoothing

²Thanks to Raúl San José Estépar for providing the ultrasound dataset.

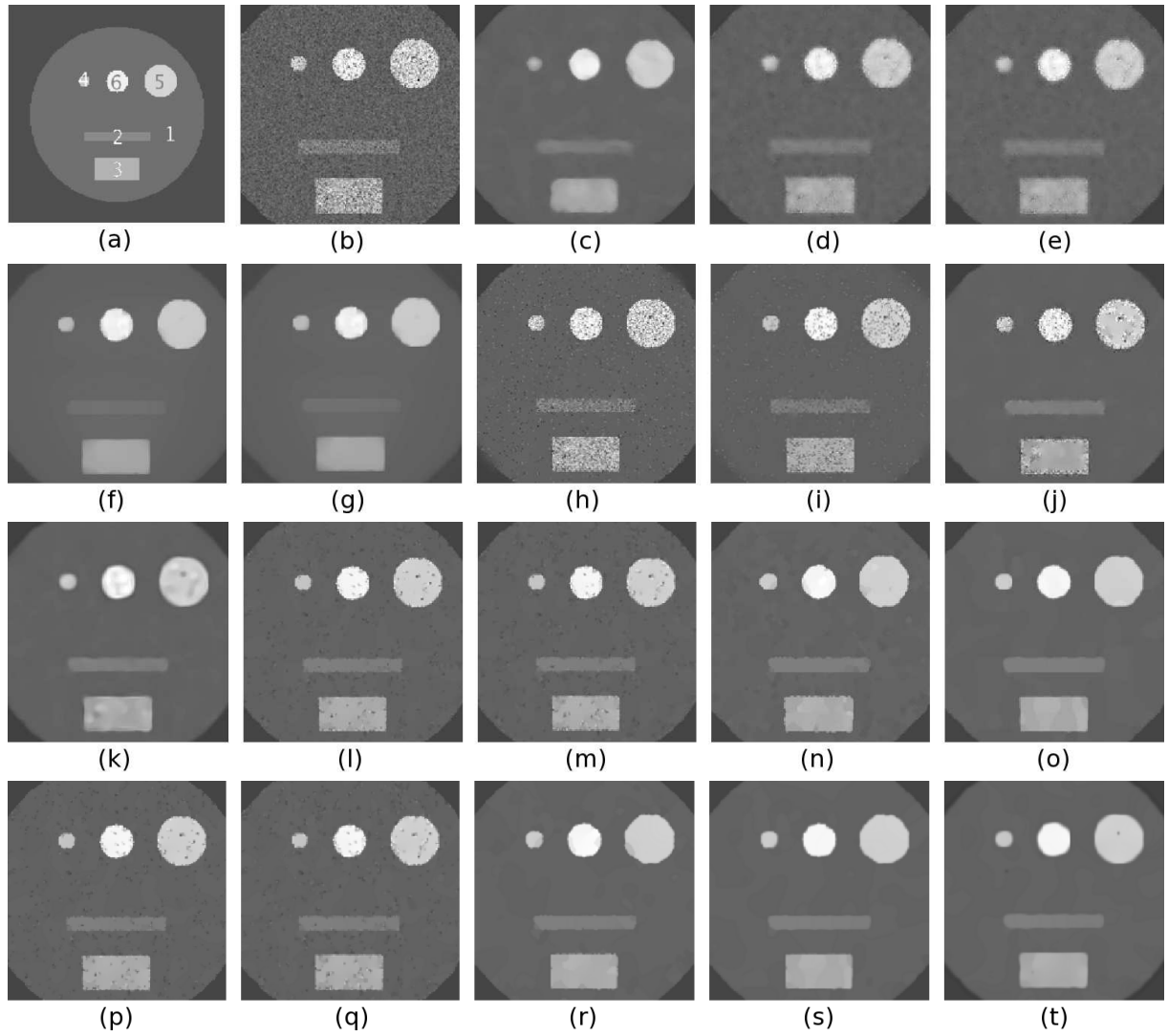


Fig. 4. Results of various filters on a multiplicative noise with $\sigma_n = 0.5$. The following filters have been applied: a) Initial synthetic 2D image with regions numbered from 1 to 5, b) Zoom on the noisy synthetic image with $\sigma_n = 0.5$, c) Median, d) Lee, e) Kuan, f) Rudin, g) Rudin att., h) Perona Malik, i) Homotopic P & M, j) Catté et al., k) Flux, l) SRAD explicit N_4 , m) SRAD explicit N_9 , n) SRAD implicit N_4 , o) SRAD implicit N_9 , p) DPAD explicit N_4 , q) DPAD explicit N_9 , r) DPAD implicit N_4 , s) DPAD implicit N_9 , t) OSRAD.

TABLE V

RESTORATION QUALITY ON NOISY SYNTHETIC 2D IMAGE WITH $\sigma_n = 0.5$, PRESENTED AS MEAN \pm STANDARD DEVIATION OF THE INTENSITY IN THE DIFFERENT REGIONS.

	R1	R2	R3	R4	R5	R6	M_f	FOM
Initial	10	20	40	50	60	80		1
Noisy image	10.03 \pm 5.00	20.26 \pm 9.57	39.39 \pm 20.23	54.86 \pm 22.09	58.72 \pm 29.55	81.12 \pm 40.59		0.193
Median	10.00 \pm 0.65	18.58 \pm 1.96	37.42 \pm 4.77	38.42 \pm 7.53	57.40 \pm 4.89	75.80 \pm 9.77	0.01	0.434
Lee	10.09 \pm 1.42	19.34 \pm 1.93	38.55 \pm 5.64	48.66 \pm 7.27	57.18 \pm 7.20	77.82 \pm 11.96	0.02	0.224
Kuan	10.11 \pm 1.42	19.33 \pm 1.90	38.53 \pm 5.47	48.64 \pm 7.26	57.13 \pm 6.93	77.71 \pm 11.52	0.02	0.222
P&M	9.97 \pm 2.39	19.95 \pm 9.10	39.38 \pm 20.17	54.90 \pm 22.02	58.72 \pm 29.53	81.12 \pm 40.58	0.00	0.323
homotopic P&M	9.55 \pm 1.53	18.56 \pm 6.00	37.80 \pm 13.56	51.46 \pm 11.37	56.31 \pm 19.87	77.85 \pm 26.69	0.00	0.533
Catté et al.	10.02 \pm 0.89	20.02 \pm 1.22	39.39 \pm 10.36	54.86 \pm 19.65	58.72 \pm 17.97	81.12 \pm 34.55	0.00	0.626
Flux	10.01 \pm 0.61	20.13 \pm 0.93	39.58 \pm 4.08	55.12 \pm 4.93	58.90 \pm 5.49	81.36 \pm 8.82	0.37	0.693
Rudin et al.	10.01 \pm 0.87	15.11 \pm 0.41	37.49 \pm 2.08	47.16 \pm 3.15	56.97 \pm 2.62	79.10 \pm 6.64	0.04	0.852
Rudin et al. attach	9.85 \pm 0.89	15.04 \pm 0.42	37.44 \pm 2.10	47.14 \pm 3.17	56.93 \pm 2.63	79.07 \pm 6.67	0.03	0.846
SRAD, expl., N_4	10.12 \pm 0.93	19.95 \pm 1.60	39.66 \pm 4.63	53.82 \pm 5.07	58.89 \pm 7.07	81.45 \pm 10.44	0.17	0.361
SRAD, expl., N_9	10.11 \pm 0.98	20.00 \pm 1.55	39.64 \pm 5.03	54.15 \pm 4.36	58.96 \pm 7.25	81.48 \pm 10.53	0.17	0.347
SRAD, impl., N_4	10.47 \pm 0.59	20.66 \pm 0.90	41.36 \pm 2.74	57.51 \pm 2.96	60.89 \pm 2.06	84.89 \pm 4.33	0.29	0.375
SRAD, impl., N_9	10.42 \pm 0.39	20.42 \pm 0.40	41.22 \pm 2.54	59.14 \pm 0.81	60.69 \pm 1.02	84.13 \pm 1.37	0.48	0.615
DPAD, expl., N_4	10.12 \pm 0.93	19.94 \pm 1.64	39.64 \pm 4.58	53.67 \pm 4.89	58.86 \pm 6.95	81.37 \pm 10.27	0.18	0.387
DPAD, expl., N_9	10.11 \pm 0.97	20.00 \pm 1.55	39.63 \pm 4.93	54.03 \pm 4.15	58.94 \pm 7.08	81.43 \pm 10.22	0.18	0.341
DPAD, impl., N_4	10.48 \pm 0.38	20.65 \pm 0.66	41.54 \pm 2.19	57.43 \pm 3.06	60.61 \pm 2.13	85.20 \pm 3.72	0.37	0.524
DPAD, impl., N_9	10.44 \pm 0.35	20.43 \pm 0.54	41.09 \pm 2.00	58.35 \pm 1.11	60.89 \pm 0.86	85.00 \pm 2.03	0.51	0.731
OSRAD	10.28 \pm 0.51	20.09 \pm 0.82	40.38 \pm 2.38	54.95 \pm 1.69	59.64 \pm 3.73	83.52 \pm 4.26	0.50	0.768

TABLE VI
RESULTS ON NOISY SYNTHETIC 2D IMAGE WITH $\sigma_n = 1$.

	R1	R2	R3	R4	R5	R6	M_f	FOM
Initial	10	20	40	50	60	80		1
Noisy image	9.99 \pm 9.97	20.22 \pm 20.83	38.94 \pm 39.97	53.37 \pm 48.59	62.72 \pm 59.94	82.31 \pm 83.00		0.198
Median	9.93 \pm 1.29	17.77 \pm 2.19	34.93 \pm 7.43	23.64 \pm 6.59	57.44 \pm 10.57	70.67 \pm 19.40	0.07	0.257
Lee	10.02 \pm 7.20	20.02 \pm 15.09	38.51 \pm 29.26	50.68 \pm 35.73	62.11 \pm 41.67	80.98 \pm 61.29	0.00	0.198
Kuan	10.04 \pm 6.15	19.95 \pm 12.84	38.36 \pm 24.94	49.70 \pm 30.27	61.91 \pm 35.75	80.35 \pm 52.11	0.00	0.197
P&M	9.97 \pm 9.35	20.20 \pm 20.78	38.94 \pm 39.97	53.37 \pm 48.58	62.72 \pm 59.94	82.31 \pm 83.00	0.00	0.199
homotopic P&M	11.56 \pm 6.63	22.20 \pm 15.28	42.24 \pm 30.87	56.15 \pm 39.70	66.08 \pm 47.36	87.20 \pm 64.03	0.00	0.197
Catté et al.	9.98 \pm 1.76	20.47 \pm 8.25	38.96 \pm 29.46	53.37 \pm 45.15	62.72 \pm 53.85	82.31 \pm 81.45	0.00	0.566
Flux	9.98 \pm 0.97	20.70 \pm 3.61	39.28 \pm 8.92	52.26 \pm 9.06	63.15 \pm 12.11	82.79 \pm 18.36	0.42	0.566
Rudin et al.	10.89 \pm 0.90	17.75 \pm 0.58	40.69 \pm 4.61	50.61 \pm 8.68	65.86 \pm 11.38	87.46 \pm 25.62	0.33	0.667
Rudin et al. attach	10.29 \pm 0.92	17.29 \pm 0.60	40.26 \pm 4.71	50.23 \pm 8.89	65.50 \pm 11.56	87.06 \pm 25.96	0.34	0.662
SRAD, expl., N_4	11.04 \pm 1.11	21.63 \pm 3.59	42.22 \pm 7.49	54.37 \pm 11.17	66.86 \pm 7.28	88.57 \pm 16.73	0.30	0.419
SRAD, expl., N_9	11.02 \pm 1.29	21.80 \pm 3.77	42.30 \pm 8.41	54.82 \pm 11.50	67.00 \pm 9.23	88.78 \pm 18.74	0.25	0.390
SRAD, impl., N_4	11.58 \pm 1.10	23.78 \pm 2.33	45.22 \pm 4.22	55.83 \pm 10.53	71.34 \pm 4.83	97.19 \pm 9.21	0.24	0.392
SRAD, impl., N_9	11.64 \pm 0.95	24.09 \pm 1.75	45.28 \pm 3.29	56.36 \pm 1.47	71.73 \pm 1.18	96.43 \pm 4.08	0.35	0.500
DPAD, expl., N_4	11.07 \pm 1.10	21.52 \pm 3.52	42.22 \pm 7.21	54.19 \pm 11.05	66.94 \pm 7.10	88.45 \pm 15.98	0.32	0.428
DPAD, expl., N_9	11.02 \pm 1.27	21.79 \pm 3.69	42.29 \pm 8.06	54.63 \pm 11.05	66.97 \pm 8.77	88.69 \pm 17.73	0.27	0.381
DPAD, impl., N_4	11.78 \pm 1.21	23.65 \pm 2.38	45.38 \pm 3.40	56.21 \pm 10.37	71.35 \pm 4.59	99.68 \pm 10.31	0.21	0.513
DPAD, impl., N_9	11.72 \pm 0.89	24.04 \pm 1.60	44.90 \pm 3.05	56.58 \pm 4.89	71.78 \pm 1.09	98.01 \pm 6.96	0.33	0.578
OSRAD	10.93 \pm 1.04	21.02 \pm 1.13	40.93 \pm 4.37	50.93 \pm 0.27	66.67 \pm 1.37	90.35 \pm 7.57	0.63	0.825

TABLE VII
PARAMETERS OF THE DIFFERENT FILTERS FOR THE SYNTHETIC 3D IMAGE.

Filter	Iter.	dt	Neighb.	Thres.	Scheme	c_{min}	c_{max}	Other
Median	4	-	N_{27}	-	-	-	-	-
Lee and Kuan	1	-	7×7	-	-	-	-	known σ_n
P&M	150	0.1	-	5	expl.	-	-	-
Homotopic P&M	400	0.1	-	0.3	expl.	-	-	-
Catté et al.	150	0.1	$\sigma = 2$	1	expl.	-	-	-
Rudin et al.	1000	0.01	-	-	expl.	-	-	-
Rudin et al. attach	3000	0.05	-	-	expl.	-	-	-
Flux diffusion	200	0.05	$\sigma = 1.5$	1	expl.	0.5	0.1	-
SRAD and DPAD	300	0.05	N_6/N_{27}	-	expl. / impl.	-	-	selected constant region
OSRAD	200	0.05	$N_{27}, \sigma = 0.7$	2	impl.	0.5	0.1	selected constant region

of standard deviation 0.7 (in voxel unit), and minimal and maximal curvature coefficients of 0.5 and 0.01 respectively. The processing time was about 30 seconds per iteration (25 minutes in total) on a Pentium Centrino processor running at 1.7 GHz, and the algorithm can be easily parallelized. In the filtered image of Fig. 6, we can appreciate the noise reduction while most structures are still present in the image. Fig. 6 right depicts the evolution of the distance between filtered images at successive iterations. This distance is computed as a root mean square of the difference between the two images. The exponential decrease of this distance shows the good convergence property of the filter.

Fig. 7 shows, on a selected region, the observed image g , the restored image \hat{f} , the estimated noise $\hat{n} = g/\hat{f}$ given our multiplicative noise model, and the local mean and standard deviation calculated on the estimated noise \hat{n} , with a $9 \times 9 \times 9$ neighborhood. If the model is correct and the filter is efficient, a close inspection should reveal that the noise is uncorrelated to the different tissues (in this case liver and vessels), and justify, a posteriori, the noise model that we used.

V. CONCLUSION AND PERSPECTIVES

We have presented a new image restoration technique, which takes into account a multiplicative model of the speckle noise in ultrasound images. This new technique combines a

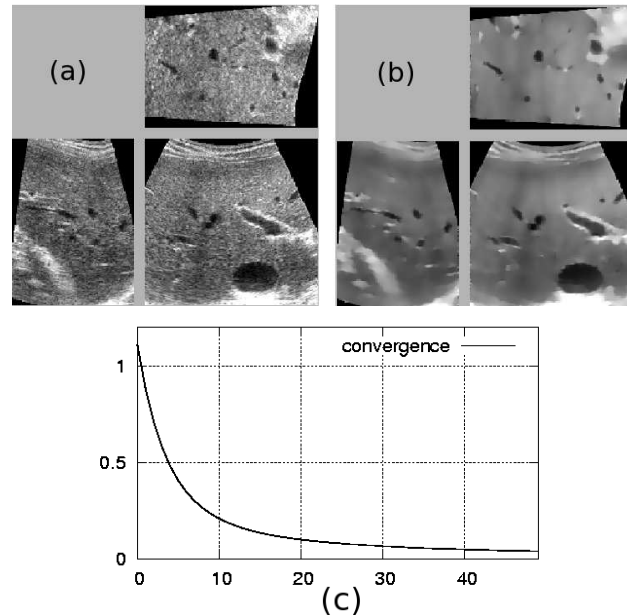


Fig. 6. a) 3D ultrasound dataset of a liver, b) result of our filter with 50 iterations. c) evolution of the distance between 2 successive images.

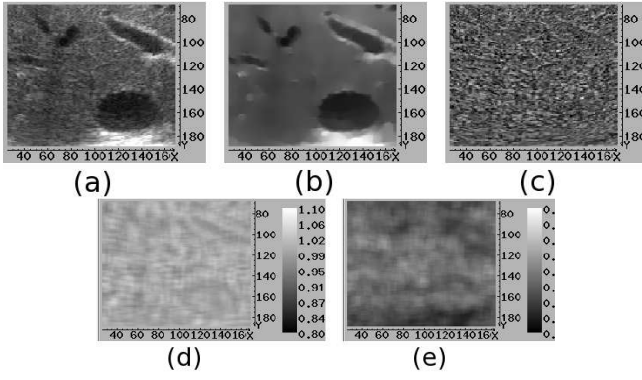


Fig. 7. Visual comparison of the noise texture between vessel and liver tissues. a) observed signal g , b) restored signal \hat{f} , c) estimated noise $\hat{n} = g/\hat{f}$, d) local mean and e) local standard deviation of the estimated noise.

matrix anisotropic diffusion method designed to preserve and enhance small vessel structures [45], and the Detail Preserving Anisotropic Diffusion [17], which is a variant of the Speckle Reducing Anisotropic Diffusion [16] specially designed to reduce multiplicative noise.

We studied the properties of the explicit numerical scheme for both SRAD and DPAD, showing under which constraint the explicit discretization of SRAD becomes stable. We proposed a semi-explicit scheme based on Jacobi method as a good tradeoff between accuracy and speed. We then extended the scalar diffusion to a matrix diffusion, applying a DPAD equation in the smoothed gradient direction and a constant diffusion in the direction of minimal curvature. We also showed that the local variance in the direction of a principal curvature is related to the principal curvature itself in (42), giving a new analogy between the local geometry and the local directional statistics in the image.

Experiments on synthetic images in two and three dimensions show the advantages of the proposed technique compared to several other filters, both in reducing the noise and in preserving and enhancing the contours.

Future work includes improving the filter by taking into account more complex statistical models of the speckle distribution, applying a pre-processing procedure to decorrelate the data as proposed in [19], comparing the performance of our technique with wavelet-based denoising proposed in [46], [47], [48], and evaluating the performance of the filter as a pre-processing tool for automatic segmentation algorithms. We plan in particular to use a level set technique for automatic segmentation of the blood vessels in the liver. Another interesting opportunity is to run intensity correction algorithms like the Expectation-Maximization algorithm proposed in [49], or algorithms based on entropy minimization[50], and ideally to include an intensity correction within our noise reduction technique.

ACKNOWLEDGEMENTS

The authors would like to thank Yu and Acton for providing their matlab code of the Speckle Reducing Anisotropic Diffusion.

APPENDIX

Relation between the local directional variance and the local geometry

A. Uniform case

a) Expression of the directional mean:

$$m_{\mathbf{v}} \approx \frac{1}{2A} \int_{-A}^A u(\mathbf{x}) + h\mathbf{v}^t \nabla u + \frac{h^2}{2} \mathbf{v}^t H \mathbf{v} dh \quad (46)$$

$$\approx u(\mathbf{x}) + \frac{A^2}{6} \mathbf{v}^t H \mathbf{v}, \quad (47)$$

where $m_{\mathbf{v}} = m_{\mathbf{v}}(u, \mathbf{x})$.

b) Expression of the directional variance: because $m_{\mathbf{v}}$ is the mean value of the image intensity along the segment $[\mathbf{x} - A\mathbf{v}, \mathbf{x} + A\mathbf{v}]$, we have the relation:

$$V_{\mathbf{v}}^1(u, \mathbf{x}) = V_{\mathbf{v}}(u, \mathbf{x}) + (u(\mathbf{x}) - m_{\mathbf{v}})^2, \quad \text{where} \quad (48)$$

$$V_{\mathbf{v}}^1(u, \mathbf{x}) = \frac{1}{2A} \int_{h=-A}^A (u(\mathbf{x} + h\mathbf{v}) - u(\mathbf{x}))^2 dh. \quad (49)$$

Using (30), we can write:

$$\begin{aligned} (u(\mathbf{x} + h\mathbf{v}) - u(\mathbf{x}))^2 &\approx \left(h\mathbf{v}^t \nabla u + \frac{1}{2} h^2 \mathbf{v}^t H \mathbf{v} \right)^2 \\ &= h^2 \left((\mathbf{v}^t \nabla u \cdot \nabla u^t \mathbf{v} + \frac{h}{2} f(\mathbf{v}, \nabla u, H) + \frac{h^2}{4} \mathbf{v}^t H \mathbf{v} \mathbf{v}^t H \mathbf{v}) \right). \end{aligned} \quad (50)$$

So we obtain the following expression for $V_{\mathbf{v}}^1$:

$$V_{\mathbf{v}}^1 = \alpha \mathbf{v}^t \nabla u \cdot \nabla u^t \mathbf{v} + \beta \mathbf{v}^t H \mathbf{v} \mathbf{v}^t H \mathbf{v}, \quad (52)$$

with $\alpha = \frac{1}{2A} \int_{h=-A}^A h^2 dh = \frac{A^2}{3}$ and $\beta = \frac{1}{2A} \int_{h=-A}^A \frac{h^4}{4} dh = \frac{A^4}{20}$.

Now, the term $(u - m_{\mathbf{v}})^2$ can be expressed as $(u(\mathbf{x}) - m_{\mathbf{v}})^2 = \frac{A^4}{36} (\mathbf{v}^t H \mathbf{v})^2$, so we obtain the expression for the local variance of the image u at the position \mathbf{x} and in the direction \mathbf{v} :

$$\begin{aligned} V_{\mathbf{v}} &= V_{\mathbf{v}}^1 - (m_{\mathbf{v}} - u(\mathbf{x}))^2 \approx \alpha \mathbf{v}^t \nabla u \cdot \nabla u^t \mathbf{v} + \beta' \mathbf{v}^t H \mathbf{v} \mathbf{v}^t H \mathbf{v}, \\ \text{with } \beta' &= \beta - \frac{A^4}{36} = \frac{A^4}{45}. \end{aligned} \quad (53)$$

B. Gaussian case

c) Expression of the directional mean:

$$m_{\mathbf{v},\sigma}(u, \mathbf{x}) = u(\mathbf{x}) + \frac{\sigma^2}{2} \mathbf{v}^t H \mathbf{v} + o(h^2), \quad (54)$$

given that $\frac{1}{\sqrt{2\pi}\sigma} \int_{h=-\infty}^{+\infty} h^2 G_{\sigma}(h) dh = \frac{1}{\sqrt{2\pi}\sigma} \int_{h=-\infty}^{+\infty} \sigma^4 G_{\sigma}''(h) + \sigma^2 G_{\sigma}(h) dh = \sigma^2$.

d) Expression of the directional variance: As in the uniform case, we can define $V_{\mathbf{v},\sigma}^1$ as the variance relative to the central voxel, and $V_{\mathbf{v},\sigma}^1 = V_{\mathbf{v},\sigma} + (u(\mathbf{x} - m_{\mathbf{v},\sigma}))^2$. Using (51), we obtain

$$V_{\mathbf{v},\sigma}^1 = \alpha_1 \mathbf{v}^t \nabla u \cdot \nabla u^t \mathbf{v} + \beta_1 \mathbf{v}^t H \mathbf{v} \mathbf{v}^t H \mathbf{v}, \quad (55)$$

with $\alpha_1 = \int h^2 G_{\sigma} = \sigma^2$, $\beta_1 = \frac{1}{4} \int h^4 G_{\sigma} = \frac{3}{4} \sigma^4$, and $\mathbf{v},\sigma = \alpha_1 \mathbf{v}^t \nabla u \cdot \nabla u^t \mathbf{v} + \beta_1' \mathbf{v}^t H \mathbf{v} \mathbf{v}^t H \mathbf{v}$, where $\beta_1' = \beta_1 - \frac{\sigma^4}{4} = \frac{1}{2} \sigma^4$. Thus, we get the equivalent of (42) in the Gaussian case:

$$\forall j \in [1, N-1], V_{\mathbf{v}_j} = \frac{\sigma^4}{2} |\nabla u|^2 \kappa_j^2. \quad (56)$$

REFERENCES

- [1] A. K. Jain, *Fundamental of Digital Processing*. Upper Saddle River, NJ, USA: Prentice-Hall, 1989.
- [2] R. F. Wagner, S. W. Smith, and J. M. Sandrik, "Statistics of speckle in ultrasound B-scans," *IEEE Trans. Sonics Ultrason.*, vol. 30, no. 3, pp. 156–163, may 1983.
- [3] R. F. Wagner, M. F. Insana, and D. G. Brown, "Statistical properties of radiofrequency and envelope-detected signals with applications to medical ultrasound," *Journal of the Optical Society of America A-Optics Image Science and Vision*, vol. 4, pp. 910–922, 1987.
- [4] E. Jakeman and P. N. Pusey, "A model for non-Rayleigh sea echo," *IEEE Trans. Antennas Propagat.*, vol. 24, no. 6, pp. 806–814, nov 1976.
- [5] E. Jakeman and R. J. A. Tough, "Generalized K distribution: A statistical model for weak scattering," *J. Opt. Soc. Am.*, vol. 4, pp. 1764–1772, 1987.
- [6] V. Dutt and J. F. Greenleaf, "Adaptive speckle reduction filter for log-compressed B-scan images," *IEEE Trans. Med. Imaging*, vol. 15, no. 6, pp. 802–813, 1996.
- [7] M. F. Insana, R. F. Wagner, B. S. Garra, D. G. Brown, and T. H. Shawker, "Analysis of ultrasound image texture via generalized Rician statistics," *Opt. Eng.*, vol. 25, no. 6, pp. 743–748, 1986.
- [8] V. Dutt and J. F. Greenleaf, "Ultrasound echo envelope analysis using a homodyned K-distribution signal model," *Ultrasonic Imaging*, vol. 16, pp. 265–287, 1994.
- [9] T. Eltoft, "Modeling the amplitude statistics of ultrasonic images," *IEEE Transactions on Medical Imaging*, vol. 25, no. 2, pp. 229–240, feb 2006.
- [10] Karmeshu and R. Agrawal, "Study of ultrasonic echo envelope based on nakagami-inverse gaussian distribution," *Ultrasound in Medicine and Biology*, vol. 32, pp. 371–376, 2006.
- [11] P. M. Shankar, "Ultrasonic tissue characterization using a generalized nakagami model," *IEEE Transactions on Ultrasonics Ferroelectrics and Frequency Control*, vol. 48, no. 4, pp. 1716–1720, mar 2001.
- [12] D. Kaplan and Q. Ma, "On the statistical characteristics of the log-compressed rayleigh signals: Theoretical formulation and experimental results," *J. Acoust. Soc. Amer.*, vol. 95, pp. 1396–1400, Mar. 1994.
- [13] V. Dutt and J. Greenleaf, "Adaptive speckle reduction filter for log-compressed b-scan images," *IEEE Trans. Med. Imaging*, vol. 15, no. 6, pp. 802–813, Dec. 1996.
- [14] A. Loupas, "Digital image processing for noise reduction in medical ultrasonics," Ph.D. dissertation, University of Edinburgh, UK, 1988.
- [15] Y. Yu and S. Acton, "Edge detection in ultrasound imagery using the instantaneous coefficient of variation," *IEEE Transactions on Image Processing*, vol. 13, no. 12, pp. 1640–1655, 2004.
- [16] —, "Speckle reducing anisotropic diffusion," *IEEE Transactions on Image Processing*, vol. 11, no. 11, pp. 1260–1270, nov 2002.
- [17] S. Aja-Fernández and C. Alberola-López, "On the estimation of the coefficient of variation for anisotropic diffusion speckle filtering," *IEEE Transactions on Image Processing*, in press, vol. 15, no. 9, pp. 2694–2701, sep 2005.
- [18] K. Z. Abd-Elmoniem, A.-B. M. Youssef, and Y. M. Kadah, "Real-time speckle reduction and coherence enhancement in ultrasound imaging via nonlinear anisotropic diffusion," *IEEE Trans Biomed Eng.*, vol. 49, no. 9, pp. 997–1014, Sep 2002.
- [19] O. V. Michailovich and A. Tannenbaum, "Despeckling of medical ultrasound images," *IEEE Transactions on Ultrasonics, Ferroelectrics and Frequency Control*, vol. 53, no. 1, pp. 64–78, jan 2006.
- [20] S. O. Choy, Y. H. Chan, and W. C. Siu, "Adaptive image noise filtering using transform domain local statistics," *Optical Engineering*, vol. 37, no. 8, pp. 2290–2296, 1998.
- [21] J. Lee, "Digital image enhancement and noise filtering using local statistics," *IEEE Trans. PAMI*, vol. 2, no. 2, pp. 165–168, 1980.
- [22] V. Frost, J. Stiles, K. Shanmugan, and J. Holzman, "A model for radar images and its application to adaptive digital filtering of multiplicative noise," *IEEE Trans. PAMI*, vol. 4, no. 2, pp. 157–166, 1982.
- [23] D. T. Kuan, A. A. Sawchuk, T. C. Strand, and C. P., "Adaptive noise smoothing filter with signal-dependent noise," *IEEE Trans. PAMI*, vol. 7, no. 2, pp. 165–177, 1985.
- [24] S. Gupta, R. Chauhan, and S. Sexana, "Wavelet-based statistical approach for speckle reduction in medical ultrasound images," *Med Biol Eng Comput.*, vol. 42, no. 2, pp. 189–92, Mar 2004.
- [25] L. Rudin, P.-L. Lions, and S. Osher, "Multiplicative denoising and deblurring: Theory and algorithms," in *Geometric Level Set Methods in Imaging, Vision and Graphics*. Springer-Verlag, 2003, ch. 6, pp. 103–120.
- [26] R. Wallis, "An approach to the space variant restoration and enhancement of images," in *Proc. Symp. on Current Mathematical Problems in Image Science*, Naval Postgraduate School, Monterey, CA, 1975.
- [27] P. Perona and J. Malik, "Scale-Space and edge detection using anisotropic diffusion," *IEEE Trans. on Pattern Anal. and Mach. Intel.*, vol. 12, no. 7, pp. 629–639, July 1990.
- [28] J. Weickert, *Anisotropic Diffusion in image processing*. Stuttgart, Germany: Teubner-Verlag, 1998.
- [29] K. Krissian, "Flux-based anisotropic diffusion applied to enhancement of 3d angiogram," *IEEE Trans. Medical Imaging*, vol. 21, no. 11, pp. 1440–1442, Nov. 2002.
- [30] N. Nordström, "Biased anisotropic diffusion - A unified regularization and diffusion approach to edge detection," *Image Vision Comput.*, vol. 8, no. 4, pp. 318–327, 1990.
- [31] S. Geman and D. Geman, "Stochastic Relaxation, Gibbs Distributions, and the Bayesian Restoration of Images," *IEEE Trans. PAMI*, vol. 6, no. 6, pp. 721–741, nov 1984.
- [32] D. Mumford and J. Shah, "Boundary detection by minimizing functionals," in *CVPR*. San Francisco: IEEE Comp. Society Press, June 1985, pp. 22–26.
- [33] L. Rudin, S. Osher, and E. Fatemi, "Nonlinear total variation based noise removal algorithms," *Physica D*, vol. 60, pp. 259–268, 1992.
- [34] K. Krissian, K. Vosburgh, R. Kikinis, and C.-F. Westin, "Speckle-constrained anisotropic diffusion for ultrasound images," in *Proceedings of IEEE Computer Society Conference on Computer Vision and Pattern Recognition*, vol. 2, San Diego CA, USA, June 2005, pp. 547–552.
- [35] G. Gerig, O. Kübler, R. Kikinis, and F. A. Jolesz, "Nonlinear anisotropic filtering of mri data," *IEEE Trans. Medical Imaging*, vol. 11, no. 2, pp. 221–232, June 1992.
- [36] J. Weickert, B. ter Haar Romeny, and M. A. Viergever, "Efficient and reliable schemes for nonlinear diffusion filtering," *IEEE Transactions on Image Processing*, vol. 7, no. 3, pp. 398–410, Mar. 1998.
- [37] J. Weickert, "Recursive separable schemes for nonlinear diffusion filters," in *Scale-Space Theory in Computer Vision (Scale-Space)*, ser. Lecture Notes in Computer Science, B. ter Haar Romeny, L. Florack, J. Koenderink, and M. Viergever, Eds., vol. 1252. Utrecht: Springer Verlag, July 1997, pp. 260–271.
- [38] —, "Coherence-enhancing diffusion filtering," *Inter. Journal of Computer Vision*, vol. 31, no. 2/3, pp. 111–127, 1999.
- [39] G. Farnéback, "Polynomial expansion for orientation and motion estimation," Ph.D. dissertation, Linköping University, Sweden, SE-581 83 Linköping, Sweden, 2002, dissertation No 790, ISBN 91-7373-475-6.
- [40] K. Krissian, J. Ellsmere, K. Vosburgh, R. Kikinis, and C.-F. Westin, "Multiscale segmentation of the aorta in 3d ultrasound images," in *25th Annual Int. Conf. of the IEEE Engineering in Medicine and Biology Society (EMBS)*, Cancun Mexico, Sept. 2003, pp. 638–641.
- [41] F. Catte, T. Coll, P. L. Lions, and J. M. Morel, "Image Selective smoothing and edge detection by nonlinear diffusion," *SIAM-JAM*, vol. 29, no. 1, pp. 182–193, Feb. 1992.
- [42] W. K. Pratt, *Digital Image Processing*. New York: Wiley, 1977.
- [43] J. Canny, "A computational approach to edge detection," *IEEE Transactions on Pattern Anal. and Machine Intell.*, vol. 8, no. 6, pp. 679–698, nov 1986.
- [44] R. San-Jose, M. Martin-Fernandez, P. Caballero-Martinez, C. Alberola-Lopez, and J. Ruiz-Alzola, "A theoretical framework to three-dimensional ultrasound reconstruction from irregularly-sample data," *Ultrasound in Medicine and Biology*, no. 2, pp. 255–269, 2003.
- [45] K. Krissian, "A New Variational Image Restoration Applied to 3D Angiographies," in *IEEE W. on Var. and Level Set Meth. in Comp. Vision*, July 2001, pp. 65–72.
- [46] X. Zong, A. F. Laine, and E. A. Geiser, "Speckle reduction and contrast enhancement of echocardiograms via multiscale nonlinear processing," *IEEE Trans. on Medical Imaging*, vol. 17, no. 4, pp. 532–540, 1998.
- [47] X. Hao, S. Gao, and X. Gao, "A novel multiscale nonlinear thresholding method for ultrasonic speckle suppressing," *IEEE Trans. on Medical Imaging*, vol. 18, no. 9, pp. 787–794, 1999.
- [48] A. Achim, A. Bezerianos, and P. Tsakalides, "Novel bayesian multiscale method for speckle removal in medical ultrasound images," *IEEE Trans. Medical Imaging*, vol. 20, no. 8, pp. 772–783, 2001.
- [49] W. M. Wells, R. Kikinis, W. E. L. Grimson, and F. Jolesz, "Adaptive segmentation of MRI data," *IEEE Transactions on Medical Imaging*, vol. 15, no. 4, pp. 429–442, aug 1996.
- [50] J.-F. Mangin, "Entropy minimization for automatic correction of intensity nonuniformity," in *IEEE Work. MMBIA*. IEEE Press, 2000, pp. 162–169.



Karl Krissian Karl Krissian received his M.S. in computer science and artificial intelligence from the university of Paris XI and the Ecole Normale Supérieure de Cachan in 1996. He received his Ph.D. degree in Computer Vision from the university of Nice-Sophia Antipolis and the INRIA in 2000. His main research topics are filtering and segmentation of three-dimensional vascular images using Partial Derivative Equations. He is currently working at the university of Las Palmas of Gran Canaria in Spain.



Carl-Fredrik Westin Carl-Fredrik Westin received the MSc degree in Applied Physics and Electrical Engineering in 1988 from Linköping University. He joined the Computer Vision Laboratory in the Department of Electrical Engineering the same year where he did research on colour, information representation, image flow, frequency estimation, filtering of uncertain and irregularly sampled data and tensor operators in image analysis. In 1991, Dr. Westin was awarded the SAAB-SCANIA prize for his work in Computer Vision. He received the LicTechn. degree on the topic of feature extraction from a tensor image description in 1991. In 1994, he graduated as Ph.D. in computer vision from Linköping University. In 1996, he joined Brigham and Women's Hospital and Harvard Medical School. In 2001, he became Director of the Laboratory of Mathematics in Imaging (LMI) in the department of radiology, and a Research Affiliate of the Artificial Intelligence Laboratory at the Massachusetts Institute of Technology.



Ron Kikinis Dr. Kikinis is the founding Director of the Surgical Planning Laboratory of the Department of Radiology, Brigham and Women's Hospital and Harvard Medical School, Boston, MA, and a Professor of Radiology at Harvard Medical School. He is the Principal Investigator of the National Alliance for Medical Image Computing (a National Center for Biomedical Computing, part of the Roadmap Initiative), and of the Neuroimaging Analysis Center (a NCRR National Resource Center). He is also the Research Director of the National Center for Image Guided Therapy which is jointly sponsored by NCRR, NCI, and NIBIB. His interests include the development of image processing algorithms and their use for enabling biomedical research. He is the author and co-author of more than 230 peer-reviewed articles. Before joining Brigham & Women's Hospital in 1988, he worked as a researcher at the ETH in Zurich and as a resident at the University Hospital in Zurich, Switzerland. He received his M.D. from the University of Zurich, Switzerland, in 1982.



Kirby Vosburgh Kirby G. Vosburgh, PhD (Member IEEE) is Associate Director of the Center for Integration of Medicine and Innovative Technology (CIMIT) in Boston, MA. He is a member of the faculty of the Harvard Medical School and the research staff at Brigham and Women's Hospital (Radiology) and Massachusetts General Hospital (Dermatology).